Scripta Materialia 162 (2019) 402–407

Contents lists available at ScienceDirect

Scripta Materialia

journal homepage: www.elsevier.com/locate/scriptamat

Improved trade-off between thermoelectric performance and mechanical reliability of Mg_2Si by hybridization of few-layered reduced graphene oxides

Gwansik Kim [a,1], Sung Wng Kim [b,1], Hyun Jun Rim [a], Hwijong Lee [a], Jeongmin Kim [a], Jong Wook Roh [c], Byung-Wook Kim [d], Kyu Hyoung Lee [a,*], Wooyoung Lee [a,*]

[a] Department of Materials Science and Engineering, Yonsei University, Seoul 03722, Republic of Korea
[b] Department of Energy Science, Sungkyunkwan University, Suwon 16419, Republic of Korea
[c] School of Nano & Materials Science and Engineering, Kyungpook National University, Gyeongsangbuk-do 37224, Republic of Korea
[d] Research and Development Division, Hyundai Motor Company, Uiwang 16082, Republic of Korea

ARTICLE INFO

Article history:
Received 11 October 2018
Received in revised form 19 November 2018
Accepted 28 November 2018
Available online xxxx

Keywords:
Nanocomposite
Thermoelectric
Mg_2Si
Reduced graphene oxides
Fracture toughness

ABSTRACT

Nanocomposites can simultaneously enhance the thermoelectric and mechanical properties of thermoelectric materials. Here, we fabricated bulks of $Mg_{1.96}Al_{0.04}Si_{0.97}Bi_{0.03}$ with monodispersed few-layered reduced graphene oxides utilizing ultrasonic-based wet chemical pulverizing-mixing and spark plasma sintering to improve unfavorable trade-off between thermoelectric performance and mechanical reliability, which is important for commercialization. An unexpected high fracture toughness of ~1.88 MPa $m^{1/2}$ was observed due to the synergetic effect of the deflection of crack propagation, bridging, and sheet pull-out mechanisms, and a high thermoelectric figure of merit ~0.6 was obtained even for a high content (3 vol.%) of reduced graphene oxides.

Silicide-based thermoelectric (TE) compounds have received much attention as potential candidates for automotive TE generators (ATEGs) owing to their low density, environmental friendliness, and competitive price. In particular, n-type Mg_2Si is the most suitable for ATEGs because it has very low density (~1.99 g/cm^3) and low material cost (~$151/kg) compared to other candidates (filled skutterudite: density ~7.8 g/cm^3 and cost ~$562/kg, half-Heusler: density ~8.5 g/cm^3 and cost ~$1988/kg) [1]. Owing to these advantages, research has focused on enhancing the TE conversion efficiency (TE figure of merit, $ZT = \sigma S^2 T/\kappa_{tot}$, where σ is the electrical conductivity, S is the Seebeck coefficient, T is the absolute temperature, and κ_{tot} is the total thermal conductivity) of Mg_2Si-based compounds, and the maximum ZT value attained was 1.2 at 700 K [2], which is comparable to those of other commercial TE compounds (filled skutterudite $Ba_{0.08}La_{0.05}Yb_{0.04}Co_4Sb_{12}$: ZT ~1.7 @ 835 K, half-Heusler $Hf_{0.75}Zr_{0.25}NiSn_{0.99}Sb_{0.01}$: ZT ~1.0 @ 873 K) [3,4]. These high ZT values of TE materials enable the generation of sufficient power for mid-to-high-temperature applications, and facilitate research on modularization and system development. A key prerequisite is to secure the lifetime of a TE system for commercialization, which is directly related with the mechanical, chemical, and thermal reliability of the TE materials at higher temperatures. Mechanical reliability is the most important parameter in the use of ATEGs owing to vibrational conditions; however, Mg_2Si-based compounds have a lower mechanical reliability (K_{Ic} ~0.82 MPa $m^{1/2}$) compared to other TE materials. The fracture toughness (K_{Ic}) of higher manganese silicide is ~1.63 MPa $m^{1/2}$, whereas those of filled skutterudite and half-Heusler are ~1.5 MPa $m^{1/2}$ and ~2.2 MPa $m^{1/2}$, respectively [5–8].

Nanocomposite (introduction of nanophases in the TE matrix) would be an effective approach to enhance the mechanical properties of the TE matrix. It also improves the electronic and/or thermal transport properties in many TE compounds. Well-designed nanophases, when introduced in a monodispersed form, are expected to improve the power factor (σS^2) owing to the carrier-filtering effect or modification of the electronic structure [2,9]. Moreover, it is possible to reduce the lattice thermal conductivity ($\kappa_{lat} = \kappa_{tot} - \kappa_{ele}$, where κ_{ele} is the electronic contribution of thermal conduction) by promoting phonon scattering even at a relatively low volume fraction of nanophases [10,11]. However, several vol.% of nanophases need to be introduced to improve the mechanical reliability, considering crack propagation [12]. Control of the characteristics of the nanophases (dimension, size, type, morphology, and intrinsic properties) will be crucial for the simultaneous improvement of TE and mechanical properties, especially in Mg_2Si-based compounds, since the mean free paths for electrons and phonons

* Corresponding authors.
E-mail addresses: khlee2018@yonsei.ac.kr (K.H. Lee), wooyoung@yonsei.ac.kr (W. Lee).
[1] These authors contributed equally.

https://doi.org/10.1016/j.scriptamat.2018.11.052
1359-6462/

are similar (~20 nm) [13]. An enhanced power factor could be obtained only in nanocomposites with a very small amount of nanophases, while nanocomposites with several vol.% of the nanophases showed severely deteriorated electronic transport properties (Table S1), as expected by theoretical calculations for nanostructured silicide-based TE materials [14].

In this respect, low-dimensional carbon-based nanomaterials such as graphene, rGO, and carbon nanotubes (CNTs) are good candidates as they can possibly lead to increased interface density as well as outstanding mechanical and electrical properties. Recently, remarkable results were reported for skutterudite-based nanocomposites; K_{Ic} and ZT values of filled skutterudites were simultaneously enhanced by the introduction of several vol.% of rGO and CNT [12,15,16].

In a previous study, we determined ZT and K_{Ic} using monodispersed Sn nanoparticles (~100 nm)-embedded $Mg_{1.96}Al_{0.04}Si_{0.97}Bi_{0.03}$. K_{Ic} improved due to the deflection of crack propagation in the presence of Sn nanoparticles at grain boundaries; however, a serious trade-off with ZT was observed mainly due to the significantly intensified carrier scattering [17]. Moreover, the interface density was found to be the key parameter to determine the K_{Ic} values of nanocomposites.

In the present study, we prepared bulk nanocomposites of $Mg_{1.96}Al_{0.04}Si_{0.97}Bi_{0.03}$ with two-dimensional few-layered rGO via an ultrasonic-based wet chemical pulverizing-mixing process to improve the unfavorable trade-off between the TE performance and mechanical reliability. Unexpected high K_{Ic} ~1.88 MPa $m^{1/2}$ was observed and simultaneously high thermoelectric figure of merit ZT ~0.6 was obtained even in the nanocomposite with 3 vol.% of rGO.

We synthesized bulk nanocomposites of Al and Bi co-doped Mg_2Si with monodispersed few-layered rGO. The matrix $Mg_{1.96}Al_{0.04}Si_{0.97}Bi_{0.03}$ powders were prepared using the up-scaled solid-state reaction synthesis technique, as described in a previous study [18,19], and rGO was synthesized using the most conventional chemical method as explained in supplementary material.

Hybrid powders of $Mg_{1.96}Al_{0.04}Si_{0.97}Bi_{0.03}$ and rGO were prepared by an ultrasonic-based wet pulverizing-mixing process using bar type sonication (Q700 Sonicator), as illustrated in Fig. 1(a). In n-hexane, $Mg_{1.96}Al_{0.04}Si_{0.97}Bi_{0.03}$ and rGO were mixed for 1 h to improve the dispersibility of rGO on a large scale (10 g/batch), and dried at 200 °C for 30 h in air.

Disc-type compacted polycrystalline bulks (25 mm in diameter and 3 mm in thickness) of the nanocomposites with 1–4 vol.% rGO were prepared using spark plasma sintering (SPS) at 1023 K for 5 min under 70 MPa in vacuum. All nanocomposites had relative densities ranging from 99% (0 vol.% rGO) to 93% (4 vol.% rGO) of the theoretical density. Phase analysis was carried out using X-ray diffraction (XRD; Ultima IV/ME 200DX, Rigaku, Japan) with CuKα radiation. The microstructure of the powders (size and distribution) and bulk nanocomposites (grain size) was observed using SEM (JEOL-7800F, JEOL Ltd., Japan), and the distribution of rGO in the bulk nanocomposites was confirmed by scanning transmission electron microscopy (STEM; JEM-ARM 200F, JEOL, Japan).

The temperature dependences of σ and S were measured using a ZEM-3 system (Ulvac, Japan) from 300 K to 873 K. Hall measurements were performed under a 1 T magnetic field in the van der Pauw configuration, and the carrier concentration (n_c) and carrier mobility (μ_{Hall}) were estimated by using the one-band model. Thermal diffusivity (λ) values were measured by the laser flash method (Netzsch LFA-457, Germany) under vacuum from 373 K to 873 K. Specific heat capacity (C_p) values were measured using differential scanning calorimetry (DSC; DSC 8000, Perkin Elmer, USA). κ_{tot} values were calculated using the equation $\kappa_{tot} = \rho_s C_p \lambda$, where ρ_s is the density.

In nanocomposite TE materials, the dispersibility of nanophases is one of the key parameters to determine both electronic and thermal transport properties. Particularly in carbon-based nanophases such as CNTs, rGO, and graphene, the dependence of TE transport properties on the dispersibility becomes more important owing to detrimental effects arising in the presence of agglomerated carbon. As shown in Table S2, well-controlled and monodispersed carbon nanophases led to enhanced TE performance in commercial TE materials. We fabricated bulk nanocomposites of $Mg_{1.96}Al_{0.04}Si_{0.97}Bi_{0.03}$ with monodispersed few-layered rGO by SPS compaction of hybrid powders of $Mg_{1.96}Al_{0.04}Si_{0.97}Bi_{0.03}$ and rGO. Notably, hybrid powders of $Mg_{1.96}Al_{0.04}Si_{0.97}Bi_{0.03}$ (~3 μm) with monodispersed few-layered rGO were obtained (Fig. 1(c)). The size of the rGO in the hybrid powders was maintained at the level of as-prepared rGO, owing to its high mechanical strength. Interestingly, $Mg_{1.96}Al_{0.04}Si_{0.97}Bi_{0.03}$ powders wrapped by rGO were observed in the hybrid powders (Fig. 1(c)).

The microstructure of the SPS-compacted bulk nanocomposites was confirmed by SEM analysis of the fractured surface. As shown in Fig. S5, grain growth during SPS was not significant; the average grain size of the bulk nanocomposites was ~3 μm, similar to that of the powder, suggesting that rGO acts as a grain growth inhibitor. Owing to the reduced grain size of the nanocomposites, the relative densities (~93%) decreased and the fraction of MgO increased compared to the pristine sample (Fig. S6) [20]. The detailed positions and morphology of the rGO in the bulk nanocomposites were obtained by TEM. TEM/EDS analysis revealed that few-layered rGO with an average thickness of ~5 nm was located at the grain boundaries (Fig. 1(d), (e)). rGO-wrapped $Mg_{1.96}Al_{0.04}Si_{0.97}Bi_{0.03}$ found in the hybrid powders was also observed in the bulk, and was similar in morphology to the nanocomposite of $Ce_yFe_3CoSb_{12}$ and rGO [15].

The temperature dependence of σ and S of the nanocomposites as a function of rGO contents was determined to investigate the effect of rGO at the grain boundaries on the electronic transport properties (Fig. 2). rGO at the grain boundaries might contribute to improving the electronic transport properties of TE materials. For example, enhanced σ has been reported in ZnO systems due to the modification of the band structure for rGO and Al-doped ZnO; a higher μ_{Hall} corresponding to those of single crystals was realized [21]. However, the σ values of the nanocomposites were lower than those of the pristine sample, and decreased with rGO content throughout the measured temperature range, suggesting that electron carriers would be scattered by rGO. To clarify this, we calculated n_c and μ_{Hall} by considering a one-band model, and have represented them in Fig. S7(a). The reduction in σ was related with the decrease in n_c (9.27×10^{19} cm^{-3} for the pristine sample, 8.82×10^{19} cm^{-3} for 1 vol.% rGO nanocomposite, and 1.92×10^{19} cm^{-3} for 4 vol.% rGO nanocomposite) due to carrier recombination, and μ_{Hall} (81.4 cm^2 V^{-1} s^{-1} for the pristine sample, 57.9 cm^2 V^{-1} s^{-1} for 1 vol.% rGO nanocomposite, and 23.6 cm^2 V^{-1} s^{-1} for 4 vol.% rGO nanocomposite) due to scattering at the interfaces between rGO and $Mg_{1.96}Al_{0.04}Si_{0.97}Bi_{0.03}$. Additionally, a sharp decrease in σ at lower temperatures occurred by the formation of MgO.

The absolute values of S slightly increased with the rGO content mainly due to the reduced n_c. However, the calculated power factor values of the bulk nanocomposites (2.39–0.62 mW m^{-1} K^{-2} for 1–4 vol.% rGO nanocomposites) were much lower than that of the pristine sample (2.72 mW m^{-1} K^{-2}). The decrease in μ_{Hall} is one reason. Another important reason for this is the unfavorable trade-off relationship between σ and S in Mg_2Si-based compounds [13,20]. Other commercial TE materials including filled skutterudite- and Bi-Te-based alloys show the general σ and S trade-off found in most TE semiconductors, yielding high power factor values in a wide n_c range. However, high power factor values can be obtained within a very narrow n_c window in Mg_2Si-based compounds, indicating that the n_c of the matrix should be tuned to the level of the maximum power factor by considering n_c variation from the nano-phases.

The temperature dependence of the κ_{tot} values of the nanocomposites as a function of rGO contents (Fig. 3(a)) was determined to investigate the effect of rGO at the grain boundaries on the thermal transport properties. The κ_{tot} values of the bulk nanocomposites (3.74–4.75 W m^{-1} K^{-1} at 373 K and 2.06–2.70 W m^{-1} K^{-1} at 873 K)

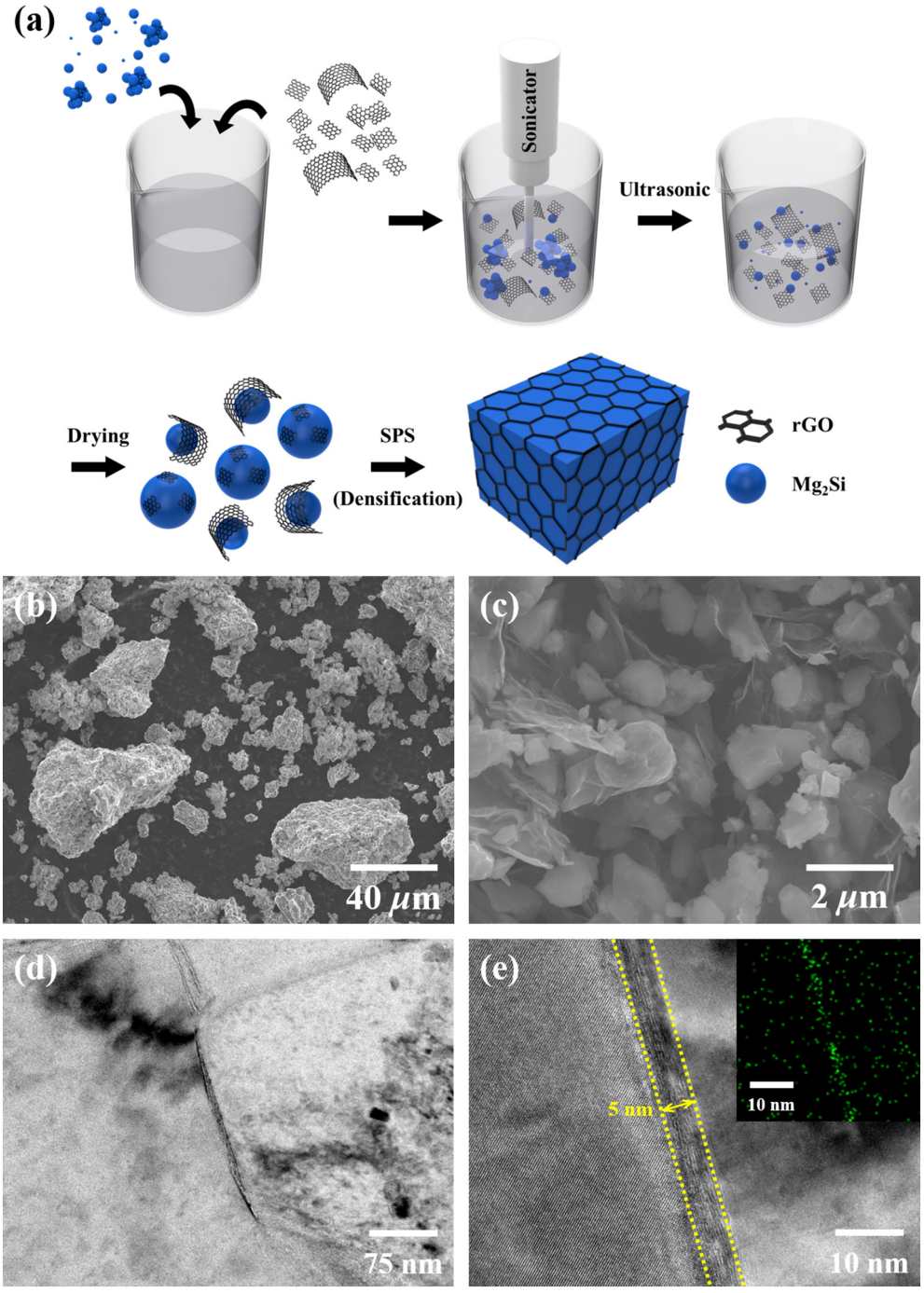

Fig. 1. (a) Schematic diagram of the ultrasonic-based wet pulverizing-mixing process, SEM images of the (b) pristine $Mg_{1.96}Al_{0.04}Si_{0.97}Bi_{0.03}$ powders and (c) hybrid powders of $Mg_{1.96}Al_{0.04}Si_{0.97}Bi_{0.03}$ and rGO with 3 vol.%, and (d, e) TEM images of the 3 vol.% rGO bulk nanocomposite. The inset in (e) shows the TEM/EDS image of the bulk nanocomposite.

were found to be lower than that of the pristine sample (5.06 W m^{-1} K^{-1} at 373 K and 2.89 W m^{-1} K^{-1} at 873 K); as the rGO content increases, κ_{tot} tends to decrease gradually. To ascertain the scattering mechanism, we calculated κ_{lat} by subtracting the electronic contribution κ_{ele} from κ_{tot}. The Lorenz number (L) was calculated as shown in the supplementary material. The bulk nanocomposites have lower κ_{lat} values compared to that of the pristine sample (Fig. 3(b)) owing to intensified phonon scattering in the presence of rGO, while a higher rGO content resulted in a rather increased κ_{lat} due to the contribution of rGO with a very high κ of ~3000 W m^{-1} K^{-1} based on the rule of mixtures (Fig. S7(b)). The estimated ZT values of the nanocomposites were lower (0.29–0.77 at 873 K) than that of the pristine sample (0.82 at 873 K) due to the decrease in power factor. However, the decrease in ZT in the rGO-introduced nanocomposites was rather moderate compared to that for the Sn nanoparticles-embedded nanocomposites [17] with the same volume fraction of nanophases (Fig. 4(c)). Reduced κ_{lat} values were obtained both in the nanocomposites with two-dimensional rGO and three-dimensional Sn nanoparticles; however, phonon scattering by the nanophases was not significant, because the main phonon scattering center in Mg_2Si is the point defect [14]. These features of the electronic and thermal transport properties suggest that rGO is more favorable than metal nanoparticles for the preparation of Mg_2Si-based nanocomposites.

The K_{Ic} values of the bulk nanocomposites are presented in Fig. 4(b). In order to analyze the effect of rGO on K_{Ic}, we used a microhardness tester to form radial cracks from the corners of the indentation. We

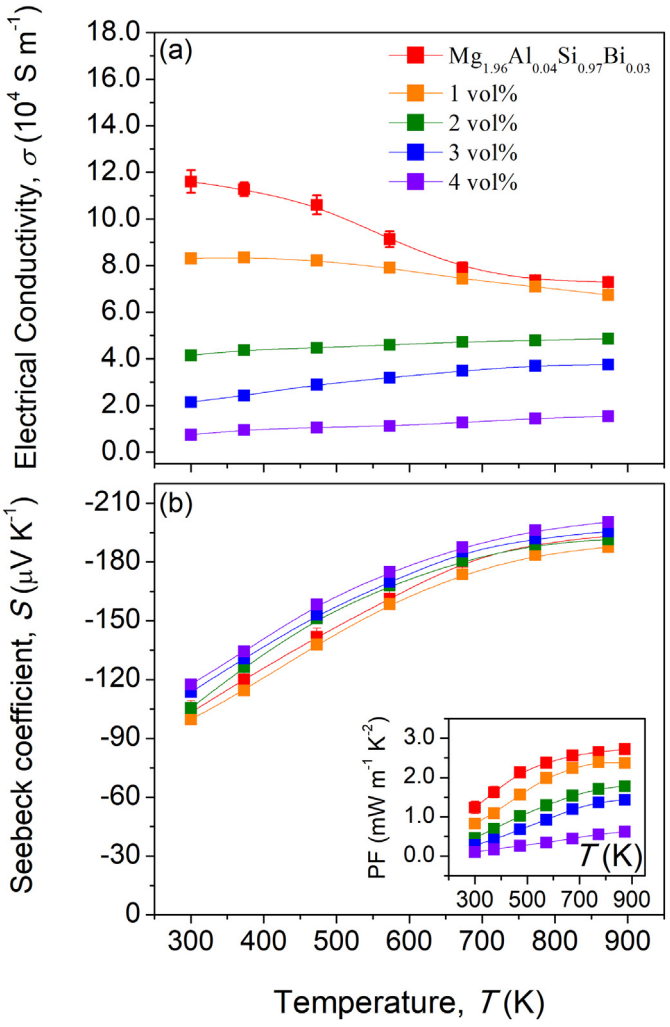

Fig. 2. Temperature dependences of (a) electrical conductivity and (b) Seebeck coefficient of the rGO bulk nanocomposites. The inset in (b) shows the temperature dependence of the power factor.

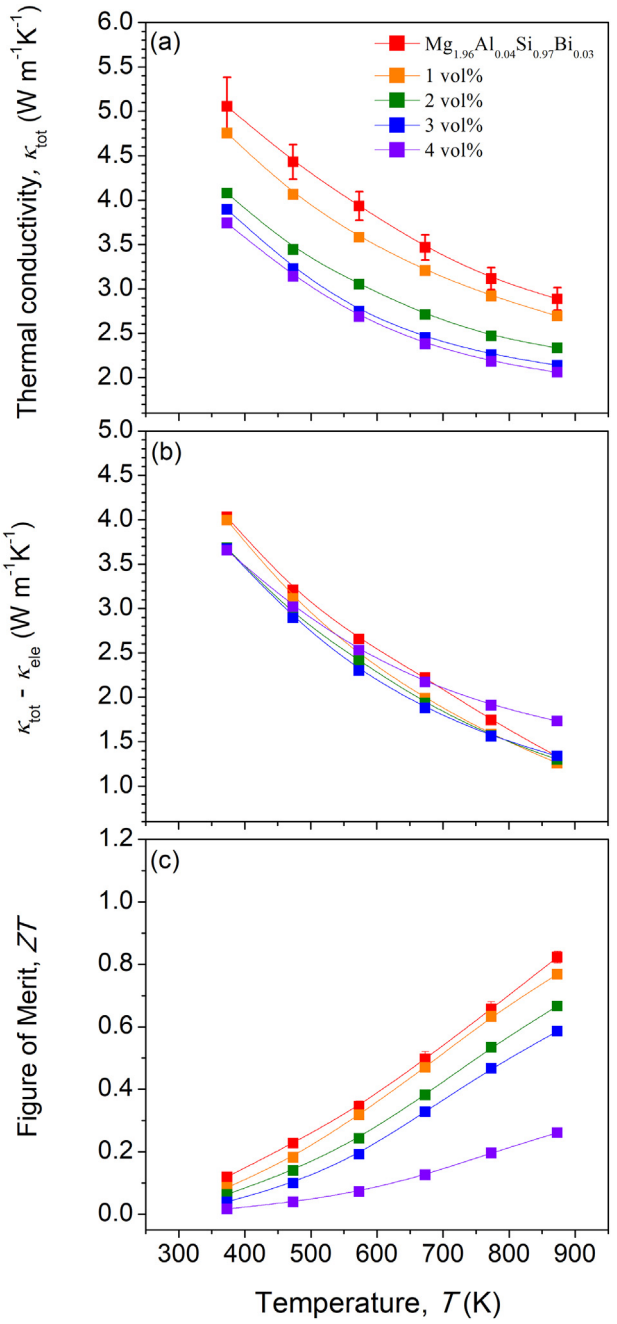

Fig. 3. Temperature dependences of (a) total thermal conductivity, (b) lattice thermal conductivity, and (c) *ZT* of the rGO bulk nanocomposites.

measured K_{Ic} at 10 different points for each sample to ensure the reliability of the measurement. The K_{Ic} values of the nanocomposites (1.12–2.06 MPa $m^{1/2}$) increased with rGO contents, and were comparable to that of the p-type counterpart higher manganese silicide (~1.63 MPa $m^{1/2}$) [5]. A microhardness indentation image of the bulk nanocomposite with 3 vol.% rGO is shown in Fig. 4(a). The insets of Fig. 4(a) show three different mechanisms for K_{Ic} enhancement; deflection of crack propagation, bridging of the crack, and sheet pull-out within the crack. The improved K_{Ic} by the deflection of crack propagation typically occurs by the introduction of any type of nanophase. The dimension of the nanophases is not important for this mechanism; instead, increase in the density of the nanophases is important. K_{Ic} enhancement by bridging the crack and sheet pull-out within the crack can only be induced by low-dimensional nanophases, since these two mechanisms arise due to the absorption of crack propagation energy. Moreover, increasing the contact area with the matrix by the introduction of two-dimensional rGO will require more energy than for a one-dimensional nanofiber [22]. Owing to the difference in K_{Ic} enhancement mechanisms with the dimensionality of the nanophases, the K_{Ic} values of the nanocomposites with two-dimensional rGO were much higher than those of nanocomposites with the three-dimensional Sn nanoparticles, especially at higher volume fraction [17].

From Fig. 4(c) and (d), we discovered an important trade-off relationship between the TE (*ZT*) and mechanical properties (K_{Ic}). We calculated $\frac{K_{Ic}}{K_{Ic,\,Min}} \times \frac{ZT}{ZT_{Max}}$, which can directly provide numerical information about this trade-off (Fig. 4(e)). Although the reduction of *ZT* by the introduction of nanophases was unavoidable, the trade-off between *ZT* and K_{Ic} was significantly improved by the controlled introduction of the few-layered rGO. We emphasize that the trade-off between *ZT* and mechanical reliability should be investigated before module and system fabrication. Our results could aid in establishing design guidelines for the development of bulk TE nanocomposites for power generation applications.

We developed Mg_2Si-based thermoelectric nanocomposites with enhanced fracture toughness (~1.88 MPa $m^{1/2}$) and a high *ZT* of 0.6 at 873 K by the introduction of 3 vol.% few-layered rGO (~5 nm in thickness). The high density of interfaces between the $Mg_{1.96}Al_{0.04}Si_{0.97}Bi_{0.03}$ matrix and two-dimensional rGO leads to significantly improved fracture toughness. Owing to the intrinsic characteristics of the electronic and thermal transport of Mg_2Si, deterioration of electronic transport

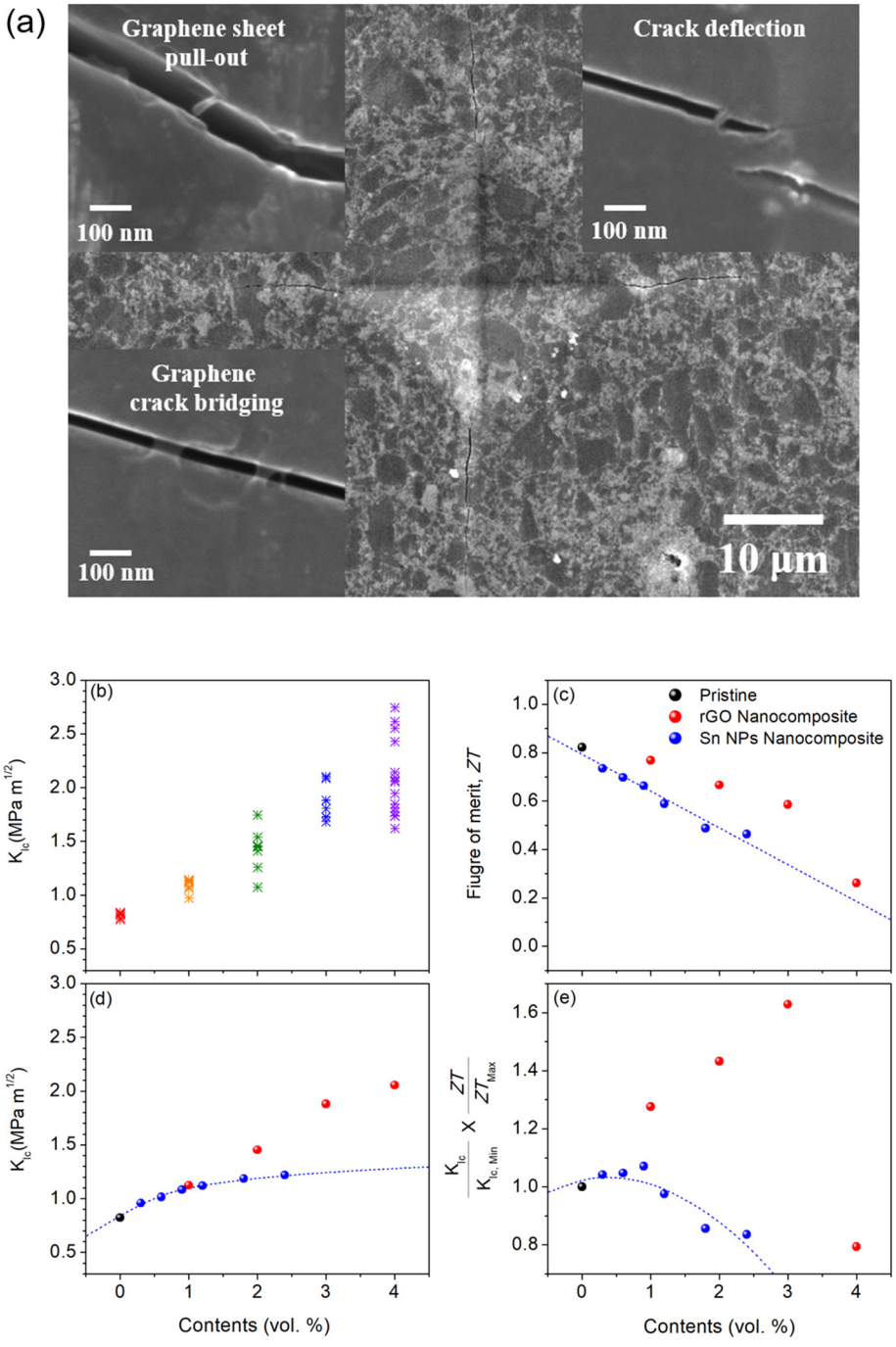

Fig. 4. (a) Toughening mechanisms in the rGO bulk nanocomposites. A microhardness indentation image of the bulk nanocomposite with 3 vol.% rGO. The insets indicate that K_{Ic} enhancement occurs by three mechanisms; deflection of crack propagation, bridging of the crack, and sheet pull-out within the crack. (b) rGO content dependence of K_{Ic} and (c) nanophase content dependence of ZT, (d) K_{Ic}, and (e) $\frac{K_{Ic}}{K_{Ic,\,Min}} \times \frac{ZT}{ZT_{Max}}$ for the nanocomposites.

properties could not be completely prevented in the presence of nanophases; however, we could significantly reduce carrier scattering by the well-controlled introduction of rGO. We also found that the carrier concentration of the Mg_2Si matrix should be tuned by considering the variation from the nanophases to obtain a high power factor in nanocomposites.

Acknowledgments

This work was supported by the National Research Foundation of Korea (NRF) grant (2017R1A2A1A17069528) funded by the Korea government (MSIT), the Industrial Fundamental Technology Development Program (10052977) funded by the Ministry of Trade, Industry and Energy (MOTIE), and Hyundai Motor Group (2017-11-0993).

Appendix A. Supplementary data

Supplementary data to this article can be found online at https://doi.org/10.1016/j.scriptamat.2018.11.052.

References

[1] U.S. Department of Energy (DOE), Thermoelectric Materials, Devices and Systems: Technology Assessment, 2015.

[2] W. Liu, X. Tan, K. Yin, H. Liu, X. Tang, J. Shi, Q. Zhang, C. Uher, Phys. Rev. Lett. 108 (2012) 166601.
[3] X. Shi, J. Yang, J.R. Salvador, M. Chi, J.Y. Cho, H. Wang, S. Bai, J. Yang, W. Zhang, L. Chen, J. Am. Chem. Soc. 133 (2011) 7837–7846.
[4] S. Chen, K.C. Lukas, W. Liu, C.P. Opeil, G. Chen, Z. Ren, Adv. Funct. Mater. 3 (2013) 1210–1214.
[5] Y. Gelbstein, J. Tunbridge, R. Dixon, M.J. Reece, H. Ning, R. Gilchrist, R. Summers, I. Agote, M.A. Lagos, K. Simpson, C. Rouaud, P. Feulner, S. Rivera, R. Torrecillas, M. Husband, J. Crossley, I. Robinson, J. Electron. Mater. 43 (2014) 1703–1711.
[6] B. Duan, P. Zhai, P. Wen, S. Zhang, L. Liu, Q. Zhang, Scr. Mater. 67 (2012) 372–375.
[7] B. Duan, P. Zhai, S. Ding, C. Xu, G. Li, L. Liu, P. Li, Q. Zhang, J. Electron. Mater. 43 (2014) 2115–2120.
[8] G. Rogl, A. Grytsiv, M. Gürth, A. Tavassoli, C. Ebner, A. Wünschek, S. Puchegger, V. Soprunyuk, W. Schranz, E. Bauer, H. Müller, M. Zehetbauer, P. Rogl, Acta Mater. 107 (2016) 178–195.
[9] J. Zhou, X. Li, G. Chen, R. Yang, Phys. Rev. B 82 (2010) 115308.
[10] S. Hwang, S.I. Kim, K. Ahn, J.W. Roh, D.J. Yang, S.M. Lee, K.H. Lee, J. Electron. Mater. 42 (2013) 1411–1416.
[11] K. Biswas, J. He, Q. Zhang, G. Wang, C. Uher, V.P. Dravid, M.G. Kanatzidis, Nature Chem. 3 (2011) 160–166.
[12] Q. Zhang, Z. Zhou, M. Dylla, M.T. Agne, Y. Pei, L. Wang, Y. Tang, J. Liao, J. Li, S. Bai, W. Jiang, L. Chen, G.J. Snyder, Nano Energy 41 (2017) 501–510.
[13] N. Satyala, D. Vashaee, J. Appl. Phys. 112 (2012) 093716.
[14] N. Satyala, D. Vashaee, Appl. Phys. Lett. 100 (2012) 073107.
[15] P. Zong, R. Hanus, M. Dylla, Y. Tang, J. Liao, Q. Zhang, G.J. Snyder, L. Chen, Energy Environ. Sci. 10 (2017) 183–191.
[16] P. Zong, X. Chen, Y. Zhu, Z. Liu, Y. Zeng, L. Chen, J. Mater. Chem. A 3 (2015) 8643–8649.
[17] G. Kim, H. Lee, H.J. Rim, J. Kim, K. Kim, J.W. Roh, S.M. Choi, B.W. Kim, K.H. Lee, W. Lee, J. Alloy. Compd. 769 (2018) 53–58.
[18] G. Kim, J. Kim, H. Lee, S. Cho, I. Lyo, S. Noh, B.W. Kim, S.W. Kim, K.H. Lee, W. Lee, Scr. Mater. 116 (2016) 11–15.
[19] G. Kim, H. Lee, J. Kim, J.W. Roh, I. Lyo, B.W. Kim, K.H. Lee, W. Lee, Scr. Mater. 128 (2017) 53–56.
[20] J. Boor, T. Dasgupta, H. Kolb, C. Compere, K. Kelm, E. Mueller, Acta Mater. 77 (2014) 68–75.
[21] W.H. Nam, B.B. Kim, S.G. Seo, Y.S. Lim, J.Y. Kim, W.S. Seo, W.K. Choi, H.H. Park, J.Y. Lee, Nano Lett. 14 (2014) 5104–5109.
[22] L.S. Walker, V.R. Marotto, M.A. Rafiee, N. Koratkar, E.L. Corral, ACS Nano 5 (2011) 3182–3190.